https://doi.org/10.62836/isrm.v3i1.0001

Global Science Publishing

ISRM

Intelligent Systems & Robotic Mechanics

https://ojs.sgsci.org/journals/isrm

Article

Autonomous Robotic Ultrasound Scanning for Liver Interventions: an Integrated Redundancy Resolution and Motion Control Framework

Peng Chen [1], Hiroshi Yokoi [1,*] and Bo Zhang [2]

[1] *Department of Mechanical and Intelligent Systems Engineering, The University of Electro-Communications, Tokyo 1828585, Japan*

[2] *Future Robotics Organization, Waseda University, Tokyo 1620044, Japan*

Featured Application: The proposed 7-DOF robotic control framework is primarily designed for autonomous ultrasound-guided liver interventional procedures, specifically for tumor puncture and thermal ablation. By ensuring sub-millimeter tracking accuracy (<0.1 mm) and high computational efficiency (approx. 720 ms), the system enables clinicians to acquire high-fidelity, repeatable ultrasound imaging, thereby reducing operator fatigue and enhancing the targeting precision of needle-based liver cancer treatments.

Abstract: Ultrasound-guided interventions, such as liver tumor puncture and ablation, are critical procedures that depend fundamentally on the acquisition of stable, high-quality, real-time imaging. Manual ultrasound scanning, however, suffers from significant operator-dependency and motion instability, which can compromise diagnostic accuracy and procedural outcomes. To address these limitations, this paper introduces a novel, integrated motion control framework for a 7-axis redundant robotic arm designed to perform automated, high-fidelity sector scans. Ultrasound-guided interventions, such as liver tumor puncture and ablation, necessitate stable and high-quality real-time imaging for procedural success. However, manual scanning is often hindered by operator dependency and inherent motion instability. This paper presents a novel motion control framework for a 7-DOF redundant robotic arm, specifically optimized for automated, high-fidelity sector scans. The methodology integrates a human-in-the-loop compliant guidance mode with an autonomous optimization-based execution scheme. The workflow enables clinicians to manually position the probe via a free-drive mode, after which the system computes a kinematically optimal trajectory by considering clinical ergonomics and joint limit avoidance. A real-time, Jacobian-based redundancy resolution controller is implemented to translate task-space trajectories into smooth joint-level commands, incorporating a null-space optimization strategy with a Clinical Dexterity & Safety Index (CDSI) to ensure avoidance of singularities and joint limits. Experimental results demonstrate that the proposed system achieves sub-millimeter tracking accuracy with a mean position error of <0.3 mm and a multi-axis orientation error of <1 deg. Furthermore, compared to standard SDK-based methods, our framework significantly enhances motion smoothness, reducing end-effector jerk by 30% and maintaining a higher directional manipulability (w_{scan}) throughout the scanning phase. This framework successfully transitions from manual guidance to automated execution, ensuring highly repeatable and stable ultrasound imaging for critical interventional procedures.

Keywords: medical robotics; autonomous ultrasound scanning; 7-DOF redundant manipulator; redundancy resolution; clinical dexterity

Received: 21 December 2025; Revised: 13 February 2026; Accepted: 26 February 2026.

* Corresponding: Hiroshi Yokoi (yokoi@mce.uec.ac.jp)

1. Introduction

Ultrasound-guided interventional procedures, particularly liver tumor puncture and thermal ablation, have established themselves as cornerstone modalities in modern interventional oncology. These minimally invasive techniques offer significant clinical advantages, including reduced patient trauma, accelerated recovery, and superior outcomes compared to traditional open surgeries [1, 2]. The clinical efficacy of such interventions is fundamentally contingent upon the acquisition of stable, high-quality, real-time ultrasound (US) imaging. These images provide the critical visualization required for precise needle trajectory guidance and the dynamic monitoring of therapeutic responses [3,4].

However, conventional free-hand ultrasound scanning remains highly operator-dependent, presenting significant challenges to procedural standardization. The quality of scanning is often limited by the sonographer's experience, operational proficiency, and physical stamina. Consequently, manual procedures frequently suffer from inconsistent image quality, poor reproducibility, and operator fatigue during prolonged interventions [5, 6]. Such limitations not only compromise diagnostic accuracy but also increase the risk of procedural complications, such as needle misplacement, thereby hindering the broader clinical adoption of these life-saving techniques [7,8].

To address these limitations, Robotic Ultrasound Scanning Systems (RUSS) have emerged as a pivotal technological solution [9]. By leveraging the inherent precision, stability, and repeatability of robotic manipulators, RUSS can automate the scanning process, effectively minimize human error and ensure the acquisition of consistent, artifact-free images—a prerequisite for reliable interventional guidance [10,11]. In this context, 7-degree-of-freedom (7-DOF) redundant robotic arms have become the research object of choice for advanced RUSS. Unlike traditional 6-DOF manipulators, 7-DOF systems offer enhanced kinematic flexibility through "self-motion" capabilities. This redundancy allows the robot to reconfigure its internal joint postures while keeping the ultrasound probe stationery at a desired pose [12,13].

This kinematic redundancy is particularly critical when navigating the complex thoracic anatomy encountered during liver interventions. In clinical practice, the human rib cage presents a significant acoustic barrier, producing dense shadows that obscure the liver parenchyma. To overcome this, sonographers typically identify a narrow intercostal space—known as an acoustic window—and perform a sector-sweep motion by pivoting the probe around a fixed point on the skin surface. This biomimetic technique allows for maximum volumetric coverage while maintaining stable acoustic coupling and avoiding rib interference. Mimicking such expert dexterity requires the robot to precisely decouple end-effector orientation from its proximal joint configurations—a task uniquely suited for 7-DOF redundant manipulators [14,15]. Furthermore, the integration of "free-drive" modes allows clinicians to manually identify these narrow acoustic windows via tactile feedback, combining human expertise with robotic precision [16].

Despite the advantages of hand-guided positioning, a significant technical gap remains in achieving a seamless, real-time transition from manual setup to autonomous scanning. Current sampling-based motion planners, such as Rapidly exploring Random Trees (RRT), often generate non-smooth trajectories and suffer from high computational latency, frequently exceeding 6 s in complex scenarios. This delay is incompatible with the real-time requirements of surgical workflows, where rapid adjustment is vital for safety and procedural efficiency [17].

To bridge this gap and meet the rigorous demands of real-time clinical interventions, this paper proposes an integrated Jacobian-based Redundancy Resolution (JDS) motion control framework. The proposed methodology is structured as a two-stage architecture: a rapid trajectory planning phase and a real-time execution phase. In the planning phase, the system parameterizes the robot's null space using a novel Clinical Dexterity & Safety Index (CDSI) to optimize joint configurations for clinical feasibility [18]. In the execution phase, a Jacobian pseudoinverse controller translates the desired sector-sweep velocity into smooth joint commands while enforcing pre-optimized configurations through null-space projection [19]. This integrated approach aims to provide a robust, high-precision solution for standardized autonomous ultrasound scanning in interventional oncology.

2. Materials and Methods

2.1. System Architecture

The integrated robotic platform (Figure 1) developed for ultrasound-guided interventions consists of three primary hardware components: an Agile Robots Diana 7 Med 7-DOF collaborative robotic arm, a custom end-effector assembly, and a standard medical ultrasound machine [20].

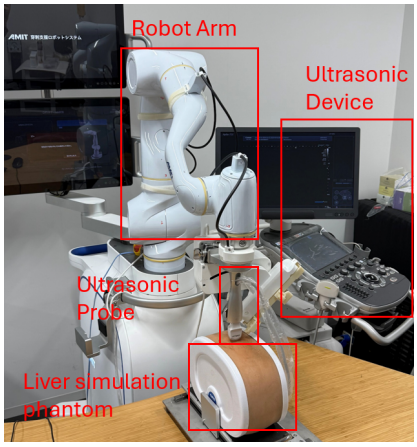

Figure 1. Experiment platform.

The Diana 7 Med features a payload of 7 kg and a declared repeatability of ±0.03 mm, which is essential for the sub-millimeter precision required in tumor biopsy and ablation procedures. A defining technical feature of this manipulator is the integration of high-resolution torque sensors within each of its seven joints. These sensors allow the system to operate with high sensitivity in compliant modes and ensure intrinsic safety during human-robot interaction [21]. The imaging component consists of a high-end Philips medical ultrasound machine (Philips Healthcare, Best, The Netherlands), which is fully integrated into the robotic control system. The end-effector is equipped with a custom-designed fixture holding a Philips convex array probe and a needle guide. This integration enables the system to perform both manual compliant scanning and autonomous trajectory execution. Clinically, the primary objective of the system is to facilitate the multi-modal registration between pre-operative CT data and real-time ultrasound imaging. By providing a stable and standardized autonomous scanning motion, the system minimizes the image deformation and inconsistency associated with manual handling, thereby improving the accuracy of anatomical alignment and subsequent lesion targeting [22]. While the initial positioning is performed by the clinician, the core contribution of this work lies in the automation of the sector scanning trajectory to ensure high-fidelity data acquisition for precision medicine.

2.2. Workflow and Task Formulation

The proposed integrated workflow for autonomous ultrasound scanning is structured into four functional phases, as illustrated in the system block diagram (Figure 2).

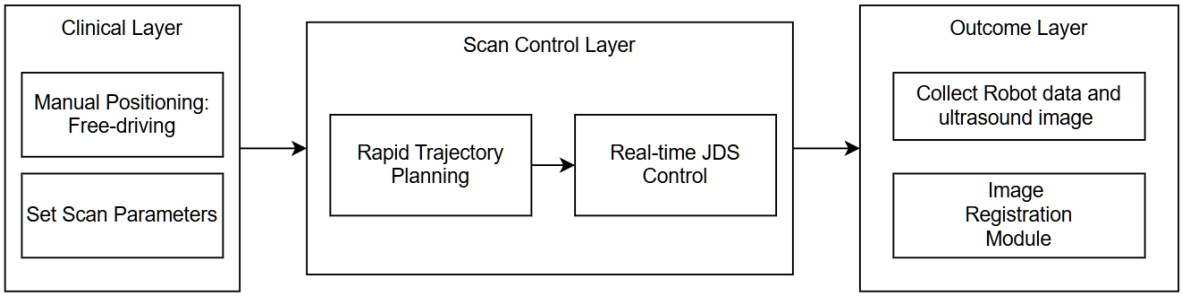

Figure 2. Workflow of Autonomous Robotic Ultrasound Scanning.

The process initiates with the Clinical Decision Layer, where the physician utilizes the robot's free-driving mode to manually guide the scan probe to the target anatomical ROI [23]. After identifying the optimal starting

pose, the physician inputs the sector scan parameters, specifically the angular range $\pm\theta_{max}$ and the scanning speed ω. This leads to the Planning Layer, where the system performs a rapid trajectory optimization. Once a kinematically feasible path is generated, the clinician provides a trigger signal via a Foot Pedal to authorize the start of the motion. During the Execution Layer, the real-time JDS controller drives the Diana 7 Med robot along the optimized arc, simultaneously acquiring synchronized streams of high-precision robot poses and ultrasound images. Finally, in the Data Fusion Layer, these real-time data streams are fed into an external registration module, where they are aligned with pre-operative CT data to facilitate multi-modal navigation for the subsequent liver intervention [24].

Geometric Definition of Sector Scanning

To maintain stable acoustic coupling and avoid rib interference, the autonomous scan is modeled as a pure rotation around a Virtual Pivot Point (VPP), denoted asP_{vpp}, located at the center of the probe's transducer surface.

A. Pivot-Point Geometric Constraint

Let $\{\mathcal{B}\}$ represent the robot base coordinate frame $\{\mathcal{T}\}$ represent the tool center point (TCP) frame located at the ultrasound probe's handle or flange. The position of the VPP in the base frame, denoted as $\boldsymbol{p}_{vpp} \in \mathbb{R}^3$, corresponds to the center of the transducer's contact surface.

At any time t during the scanning process, the relationship between the TCP position $\boldsymbol{p}_{tcp}(t)$ and the stationary VPP is governed by the following geometric constraint:

$$\boldsymbol{p}_{tcp}(t) = \boldsymbol{p}_{vpp} + \boldsymbol{R}(t) \cdot \boldsymbol{r}_{off} \tag{1}$$

$\boldsymbol{p}_{tcp}(t)$: The instantaneous Cartesian position of the probe's TCP in the base frame.

$\boldsymbol{p}_{vpp}$: The constant position of the Virtual Pivot Point in the base frame, determined during the manual positioning phase.

$\boldsymbol{R}(t)$: The 3×3 rotation matrix representing the orientation of the probe frame $\{\mathcal{T}\}$relative to the base frame $\{\mathcal{B}\}$.

$\boldsymbol{r}_{off}$: The fixed offset vector from the VPP to the TCP, defined in the probe's local coordinate system.

B. Differential Kinematics for Sector Motion

To achieve a smooth scan, the linear velocity $\boldsymbol{v}_d$ and angular velocity $\boldsymbol{\omega}_d$ of the probe must be intrinsically coupled. For a pure rotation around the stationary VPP, the following differential constraint must be satisfied:

$$\boldsymbol{v}_d = \boldsymbol{\omega}_d \times (\boldsymbol{p}_{vpp} - \boldsymbol{p}_{tcp}) \tag{2}$$

$\boldsymbol{v}_d$: The desired linear velocity vector (3×1) of the TCP.

$\boldsymbol{\omega}_d$: The desired angular velocity vector (3×1) of the TCP.

$(\boldsymbol{p}_{vpp} - \boldsymbol{p}_{tcp})$: The time-varying lever arm vector pointing from the probe's TCP to the pivot point.

C. Task-Space Velocity Command

In the JDS framework, the target task-space velocity vector $\dot{x}_d$ is specified to ensure the robot mimics the hand-pivoting motion of a sonographer:

$$\dot{x}_d = \begin{bmatrix} (\hat{\boldsymbol{k}}\dot{\theta}) \times (\boldsymbol{p}_{vpp} - \boldsymbol{p}_{tcp}) \\ \hat{\boldsymbol{k}}\dot{\theta} \end{bmatrix} \tag{3}$$

$\dot{x}_d$: The 6×1 desired velocity vector in task space, serving as the input for the subsequent Jacobian-based controller.

$\hat{\boldsymbol{k}}$: The unit vector defining the axis of rotation for the sector sweep.

$\dot{\theta}$: The scalar angular scanning speed, which determines the frame rate and temporal resolution of the acquired ultrasound sequence.

2.3. Stage 1: Rapid Trajectory Planning (Offline Phase)

The primary challenge in automating the sector scan is determining an optimal kinematic posture that ensures a smooth, collision-free, and highly dexterous sweep. Based on the standard clinical protocols defined by our collaborating physicians, the scanning range is established as $\pm 15^{\circ}$. This specific amplitude is required to maximize

the Field of View (FOV) for liver tumor visualization while operating within the geometric constraints of the intercostal acoustic window. To achieve this, we propose an offline trajectory planning algorithm based on discrete null-space sampling and multi-objective Clinical Dexterity & Safety Index (CDSI) evaluation.

2.3.1 Discretization and Motion Set Construction

To evaluate the continuous scanning motion, the desired $\pm 15^{\circ}$ sector arc is uniformly discretized into a set of five key evaluation angles:

$$\Theta = \{-15^{\circ}, -7.5^{\circ}, 0^{\circ}, 7.5^{\circ}, 15^{\circ}\} \tag{4}$$

For the starting position of the scan (-15°), the redundant null-space is uniformly sampled across N different arm angles, $\psi_j \in [-\frac{\pi}{2}, \frac{\pi}{2}](j = 1, 2, \ldots, N)$. For each candidate arm angle ψ_j, the inverse kinematics (IK) are computed for all five angles in Θ. This generates N candidate motion paths, where the path $\mathcal{Q}_j$ is defined as:

$$\mathcal{Q}_j = \{\boldsymbol{q}_{k,j} \mid \boldsymbol{q}_{k,j} = f_{IK}(\boldsymbol{x}(\theta_k), \psi_j), \theta_k \in \Theta\} \tag{5}$$

2.3.2 Multi-Objective Evaluation via CDSI

To select the optimal path from the candidate set, each path $\mathcal{Q}_j$ is evaluated against four specific indices designed for clinical robotic ultrasound.

Index 1: Motion Amplitude Minimization (I_{amp})

To ensure that the scanning motion requires the minimum possible joint effort and remains close to the initial manual posture $\boldsymbol{q}_{init}$, the cumulative deviation is calculated:

$$\boldsymbol{I}_{amp}(\boldsymbol{j}) = \sum_{k=1}^{5} \| \boldsymbol{q}_{k,j} - \boldsymbol{q}_{init} \|^2 \tag{6}$$

$\boldsymbol{q}_{init} \in \mathbb{R}^7$: The initial joint configuration vector recorded at the moment the clinician releases the "Free-drive" button.

$\boldsymbol{q}_{k,j}$: The joint configuration for the k-th evaluation angle ($\theta \in \Theta$) using the j-th candidate arm angle.

$\| \cdot \|^2$: The squared Euclidean norm (L2 norm), representing the energy or "distance" of the joint displacement.

Index 2: Task-Specific Manipulability (I_{mani})

To accurately evaluate the robot's dexterity during a sector sweep, we define the task-specific manipulability w_{scan}. Unlike the global manipulability index, w_{scan} quantifies the manipulator's ability to generate velocity specifically along the desired scanning direction.

Task Direction Vector Formulation:

For a sector scan centered at the pivot point $\boldsymbol{p}_{vpp}$and rotating around a local axis $\hat{\boldsymbol{k}}$, the required task-space velocity vector $\dot{x} \in \mathbb{R}^6$ is determined by the geometric coupling of rotation and translation. We define the normalized task direction vector $\boldsymbol{u}(\boldsymbol{q})$ as:

$$\boldsymbol{u}(\boldsymbol{q}) = \frac{\boldsymbol{a}(\boldsymbol{q})}{\| \boldsymbol{a}(\boldsymbol{q}) \|}, \quad \boldsymbol{a}(\boldsymbol{q}) = \begin{bmatrix} \hat{\boldsymbol{k}} \times (\boldsymbol{p}_{vpp} - \boldsymbol{p}_{tcp}(\boldsymbol{q})) \\ \hat{\boldsymbol{k}} \end{bmatrix} \tag{7}$$

$\boldsymbol{a}(\boldsymbol{q})$: The unnormalized velocity vector representing the 6-DOF task requirement (3D linear velocity and 3D angular velocity).

$\hat{\boldsymbol{k}}$: The unit vector of the rotation axis (e.g., $[0,\ 1,\ 0]^T$ for a sweep around the probe's y-axis).

$(\boldsymbol{p}_{vpp} - \boldsymbol{p}_{tcp})$: The lever arm from the probe's TCP to the pivot point.

Directional Manipulability Calculation:

The full Jacobian matrix $\boldsymbol{J}(\boldsymbol{q}) \in \mathbb{R}^{6 \times 7}$ maps the joint velocities to the 6-DOF end-effector velocities (three translational and three rotational). To focus on the dexterity relevant to the sector scan, the task-specific Jacobian $\boldsymbol{J}_{scan}$ is calculated as follows:

$$\boldsymbol{J}_{scan}(\boldsymbol{q}) = \boldsymbol{u}(\boldsymbol{q})^T \boldsymbol{J}(\boldsymbol{q}) \tag{8}$$

The directional manipulability index w_{scan} is then defined as the Euclidean norm of this projected Jacobian, which represents the maximum velocity the robot can achieve in the specified scanning direction for a unit joint velocity:

$$\boldsymbol{w}_{scan}(\boldsymbol{q}) = \sqrt{\boldsymbol{J}_{scan}(\boldsymbol{q})\boldsymbol{J}_{scan}(\boldsymbol{q})^T} \tag{9}$$

It is critical to avoid kinematic singularities, particularly in the direction of the sector sweep. This index evaluates the task-specific manipulability w_{scan} across the five key postures:

$$I_{mani}(j) = \frac{1}{5}\sum_{k=1}^{5}\sqrt{w_{scan}(\boldsymbol{q}_k)} \tag{10}$$

Index 3: Pitch Joint Verticality (I_{ergo})

To maximize the workspace clearance between the robotic arm and the patient's body, the second joint (q_2, representing the main pitch axis of Diana 7 Med) should be maintained as vertical as possible ($q_{2,vert}$):

$$I_{ergo}(j) = \sum_{k=1}^{5}|q_{2,k,j} - q_{2,vert}| \tag{11}$$

Index 4: Joint Limit Margin (I_{lim})

To guarantee mechanical safety throughout the continuous motion, this index penalizes configurations where any joint i approaches its hardware limits ($q_{i,min}$,$q_{i,max}$):

$$I_{lim}(j) = \sum_{k=1}^{5}\sum_{i=1}^{7}\frac{1}{(q_{i,max} - q_{i,k,j})(q_{i,k,j} - q_{i,min})} \tag{12}$$

2.3.3 Normalization and Optimal Path Selection

To ensure that all four evaluation indices contribute consistently to the optimization objective, a normalization process is applied to map each index to a dimensionless scale [0, 1], where a value of 0 represents the most desirable state and 1 represents the least desirable.

For the cost-based indices (Motion Amplitude $\boldsymbol{I}_{amp}$, Pitch Verticality $\boldsymbol{I}_{ergo}$, and Joint Limit Margin $\boldsymbol{I}_{lim}$, the standard Min-Max normalization is employed:

$$\bar{\boldsymbol{I}}_{cost}(\boldsymbol{j}) = \frac{\boldsymbol{I}(\boldsymbol{j}) - \boldsymbol{I}_{min}}{\boldsymbol{I}_{max} - \boldsymbol{I}_{min}} \tag{13}$$

For the benefit-based index (Task-Specific Manipulability $\boldsymbol{I}_{mani}$, where a higher value is preferred, the normalization is inverted to align with the "lower-is-better" logic:

$$\bar{\boldsymbol{I}}_{mani}(\boldsymbol{j}) = \frac{\boldsymbol{I}_{max} - \boldsymbol{I}_{mani}(\boldsymbol{j})}{\boldsymbol{I}_{max} - \boldsymbol{I}_{min}} \tag{14}$$

The final Clinical Dexterity & Safety Index (CDSI) score $S(j)$ for the j-th candidate arm angle is calculated as the weighted sum of these normalized components:

$$\boldsymbol{S}(\boldsymbol{j}) = \boldsymbol{w}_1\bar{\boldsymbol{I}}_{amp}(\boldsymbol{j}) + \boldsymbol{w}_2\bar{\boldsymbol{I}}_{mani}(\boldsymbol{j}) + \boldsymbol{w}_3\bar{\boldsymbol{I}}_{ergo}(\boldsymbol{j}) + \boldsymbol{w}_4\bar{\boldsymbol{I}}_{lim}(\boldsymbol{j}) \tag{15}$$

where w_1, w_2, w_3, w_4 are the respective weight coefficients determined by clinical priorities.

The comprehensive CDSI score $S(j)$ is formulated as a weighted sum. The optimal candidate index j^* is determined by minimizing the total cost:

$$\boldsymbol{j}^* = \boldsymbol{argmin}_{j\in[1,N]}\big(\boldsymbol{S}(\boldsymbol{j})\big) \tag{16}$$

The "Optimal Arm Angle" ψ^* is defined as the specific value from the sampling set ψ that minimizes the total cost function $S(j)$:

$$\boldsymbol{\psi}^* = \boldsymbol{\psi}_{j^*} \tag{17}$$

By selecting ψ^* through this comprehensive evaluation of the five-point motion set, we ensure that the resulting trajectory is not just optimal for a single point, but provides a dexterous corridor for the entire $\pm 15^\circ$ sweep. This constant ψ^*effectively "freezes" the 7th degree of freedom in a configuration that maximizes safety and clinical clearance, allowing the real-time Jacobian controller to focus exclusively on the high-precision Cartesian tracking of the probe.

2.3.4 Target State Formulation for Real-Time Control

After determining the optimal arm angle ψ^* [25] in the planning phase, the system must establish a trajectory roadmap that connects the robot's current state to the autonomous scanning sequence. This process involves formulating transition waypoints and performing a discrete verification to ensure that the path is free

from kinematic discontinuities, such as joint flips or workspace singularities [26].

A. Transition Segment Formulation (from 0° to -15°)

The transition begins at the robot's current configuration $\boldsymbol{q}_{curr}$, which corresponds to the task-space center pose $\boldsymbol{x}(0^\circ)$ manually determined by the clinician. To ensure a predictable approach to the scan's starting boundary, an intermediate checkpoint is established at the -7.5° task-space position.

The target joint configurations for the transition are calculated using the optimized arm angle ψ^*, ensuring the robot adopts the ideal redundant posture during the approach:

$$\boldsymbol{q}^*_{-7.5^\circ} = \boldsymbol{f}_{IK}(\boldsymbol{x}(-7.5^\circ), \boldsymbol{\psi}^*) \tag{18}$$

$$\boldsymbol{q}^*_{-15^\circ} = \boldsymbol{f}_{IK}(\boldsymbol{x}(-15^\circ), \boldsymbol{\psi}^*) \tag{19}$$

This strategy ensures that as the robot moves from $\boldsymbol{q}_{curr}$ to the scan origin, it smoothly converges toward the clinical safety manifold defined by the CDSI.

B. Discrete Trajectory Continuity Check

To prevent control instability during high-frequency execution (Stage 2), the planner performs a discrete sweep of the entire path—including both the transition segment $[0^\circ, -15^\circ]$and the active scan segment $[-15^\circ, +15^\circ]$. The path is sampled at a fine interval $\Delta\theta$ (e.g., 0.5°). For each sample m, the feasibility is verified by:

$$\boldsymbol{q}_m = \boldsymbol{f}_{IK}(\boldsymbol{x}(\boldsymbol{\theta}_m), \boldsymbol{\psi}^*), \quad \boldsymbol{\theta}_m \in [0^\circ, -15^\circ] \cup [-15^\circ, 15^\circ] \tag{20}$$

The sequence is considered kinematically continuous if the maximum joint-space displacement between any two consecutive samples remains below a predefined safety threshold σ:

$$\boldsymbol{max}_{i=1\ldots7} |\boldsymbol{q}_{i,m} - \boldsymbol{q}_{i,m-1}| < \boldsymbol{\sigma} \tag{21}$$

If any sample fails this check or returns no IK solution, the planner flags a "Kinematic Obstruction" and prompts the user to re-adjust the initial pose.

Once the discrete roadmap $\{\boldsymbol{q}_{curr}, \boldsymbol{q}^*_{-7.5^\circ}, \boldsymbol{q}^*_{-15^\circ}, \ldots, \boldsymbol{q}^*_{0^\circ}\}$ is validated, it is transmitted to the Stage 2 controller. As detailed in Section 2.4, the system will no longer rely on static IK solutions but will use a Jacobian-based Redundancy Resolution (JDS) scheme to resolve joint velocities $\dot{\boldsymbol{q}}$ in real-time, enabling the probe to track the target arc with sub-millimeter precision.

2.4. Stage 2: Real-Time Jacobian-Based Redundancy Resolution (JDS) Control

After establishing the optimal arm angle ψ^* and spatial waypoints in the offline planning phase (Stage 1), the system transitions to the real-time execution phase (Stage 2). To satisfy the clinical requirements for uniform and smooth ultrasound scanning, this section proposes a control framework integrating real-time task-space velocity planning, closed-loop Jacobian-based redundancy resolution (JDS), and proportional joint velocity scaling. This controller dynamically generates safe joint velocity commands at a control frequency of 1 kHz.

2.4.1 Real-Time Task-Space Velocity Planning

Since the discrete planner only provides spatial sequences, the real-time desired task-space velocity $\dot{x}_d(t)$ must be dynamically generated in the time domain. To ensure uniform acoustic sampling for 3D ultrasound reconstruction, a trapezoidal velocity profile is applied to the scanning angle $\theta(t)$ with a target constant angular velocity ω_{scan} and constant acceleration α [27].

To eliminate tracking lag and cumulative errors inherent in the robot's physical execution, a closed-loop position feedback term is integrated. Based on the current Cartesian pose $x(t)$ acquired from the SDK, the effective task-space control velocity $\boldsymbol{v}_e$ is constructed:

$$\boldsymbol{v}_e = \dot{\boldsymbol{x}}_d(\boldsymbol{t}) + \boldsymbol{K}_p(\boldsymbol{x}_d(\boldsymbol{t}) - \boldsymbol{x}(\boldsymbol{t})) \tag{22}$$

$x_d(t)$, $x(t)$: The desired and actual Cartesian poses (position and orientation) of the end-effector.

$\boldsymbol{K}_p$: A positive-definite diagonal gain matrix used to regulate the convergence rate of the Cartesian tracking error.

2.4.2 JDS Control Law Formulation

Upon formulating the task-space command $\boldsymbol{v}_e$, the system utilizes the current geometric Jacobian matrix

$\boldsymbol{J}(\boldsymbol{q}) \in \mathbb{R}^{6\times 7}$ to map the Cartesian velocity to the joint-space velocity $\dot{\boldsymbol{q}}_c$. This is achieved via the Moore-Penrose pseudoinverse $\boldsymbol{J}^{\dagger}$. Simultaneously, the optimized ideal posture feedback is introduced using the null-space projection operator:

$$\dot{\boldsymbol{q}}_c = \boldsymbol{J}^{\dagger}(\boldsymbol{q})\boldsymbol{v}_e + (\boldsymbol{I}_{7\times 7} - \boldsymbol{J}^{\dagger}(\boldsymbol{q})\boldsymbol{J}(\boldsymbol{q}))\dot{\boldsymbol{q}}_0 \tag{23}$$

$\dot{q}_c \in \mathbb{R}^7$: The vector of commanded joint velocities sent to the robot SDK.

$\boldsymbol{J}^{\dagger}(\boldsymbol{q}) = \boldsymbol{J}^T(\boldsymbol{J}\boldsymbol{J}^T)^{-1}$: The Moore-Penrose pseudoinverse of the Jacobian, which provides the minimum-norm joint velocity solution for a given task velocity.

$(\boldsymbol{I} - \boldsymbol{J}^{\dagger}\boldsymbol{J})$: The null-space projection matrix, which filters out joint motions that would disturb the end-effector's Cartesian pose.

The secondary task velocity $\dot{\boldsymbol{q}}_0$ acts as an attractive field, pulling the robot toward the optimal configurations determined in Stage 1 without disturbing the primary scanning trajectory:

$$\dot{\boldsymbol{q}}_0 = \boldsymbol{k}_{null}(\boldsymbol{q}^*(\boldsymbol{\theta}(\boldsymbol{t})) - \boldsymbol{q}) \tag{24}$$

$\dot{q}_0 \in \mathbb{R}^7$: The secondary joint velocity vector (Secondary Task).

$\boldsymbol{q}^*(\theta(t))$: The real-time reference joint posture, calculated dynamically via inverse kinematics $f_{IK}(\boldsymbol{x}_d(t), \psi^*)$ using the optimal arm angle ψ^*.

k_{null}: The scalar gain governing the null-space attraction rate.

2.4.3 Joint Velocity Saturation and Proportional Scaling

In medical interventions, strictly limiting the manipulator's operational speed is paramount for intrinsic safety. Although the planning phase optimizes motion smoothness, the JDS resolution can still produce transient peak joint velocities exceeding the system's safety threshold $\dot{q}_{limit}$, particularly when approaching singular regions or correcting large feedback errors.

A simple single-joint truncation (i.e., clamping only the speeding joint to its maximum limit) would alter the direction of the joint velocity vector $\dot{\boldsymbol{q}}_c$. This distortion would cause the actual Cartesian motion to deviate from the prescribed trajectory, violating the VPP constraint—a highly dangerous scenario during ultrasound-guided punctures.

Therefore, a proportional velocity scaling strategy is implemented. Before sending the commands to the low-level SDK, the maximum absolute velocity among the computed joints $\dot{\boldsymbol{q}}_c = [\dot{q}_{c,1}, \ldots, \dot{q}_{c,7}]^T$ is evaluated:

$$\dot{\boldsymbol{q}}_{\mathbf{max\_actual}} = \boldsymbol{max}_{i\in\{1\ldots7\}}|\dot{\boldsymbol{q}}_{c,i}| \tag{25}$$

A dynamic safety scaling factor η is then computed. If the maximum calculated velocity exceeds the safety threshold $\dot{\boldsymbol{q}}_{limit}$, the entire joint velocity vector is scaled down proportionally; otherwise, it remains unmodified:

$$\boldsymbol{\eta} = \begin{cases} \dfrac{\dot{\boldsymbol{q}}_{limit}}{\dot{\boldsymbol{q}}_{max\_actual}}, & \textbf{if } \dot{\mathbf{q}}_{max\_actual} > \dot{\boldsymbol{q}}_{limit} \\ 1, & \textbf{otherwise} \end{cases} \tag{26}$$

The final safe execution velocity $\dot{\boldsymbol{q}}_{safe}$ transmitted to the robot's hardware controller is:

$$\dot{\boldsymbol{q}}_{safe} = \boldsymbol{\eta} \cdot \dot{\boldsymbol{q}}_c \tag{27}$$

By introducing this mechanism, the system guarantees absolute joint speed compliance through global deceleration in extreme cases, while perfectly preserving the proportional relationship between all joints. This ensures the geometric integrity of the sector scan and the VPP constraint are strictly maintained, maximizing the safety and fidelity of the procedure.

3. Experiments and Results

To validate the clinical efficacy, safety, and precision of the proposed CDSI-optimized JDS control framework, comprehensive experiments were conducted on the Diana 7 Med robotic platform. The experimental design was specifically tailored to replicate the clinical workflow of ultrasound-guided liver interventions, focusing on the system's ability to maintain the Virtual Pivot Point (VPP) constraint while maneuvering through restricted intercostal spaces.

3.1. Experimental Setup and Clinical Trajectory Definition

Although in vivo human trials are currently outside the scope of this hardware validation, the experimental setup was rigorously designed to replicate clinical reality. A high-fidelity tissue-mimicking phantom was used to represent the human abdominal region. To ensure anatomical relevance, the scanning poses employed in the experiments were derived directly from preoperative 3D CT data. Experienced clinicians manually positioned virtual ultrasound probes within the CT reconstruction to target standard liver windows, and these expert-defined poses were subsequently mapped to the robotic system for execution on the phantom (Figure 3).

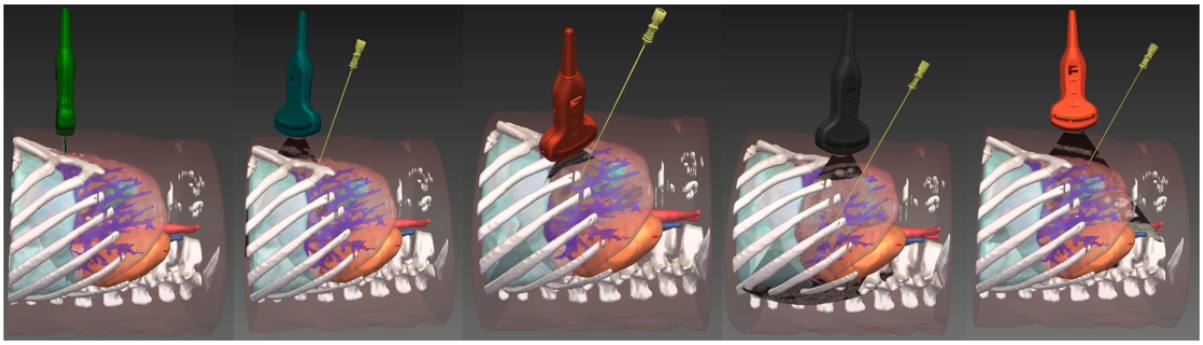

Figure 3. 3D rendering of predefined ultrasound scanning poses for simulated liver interventions.

To ensure the experimental trajectories accurately reflect real-world clinical challenges, six representative ultrasound scanning locations were derived from pre-operative 3D Computed Tomography (CT) models of the human thorax and liver. While the target Cartesian poses were directly mapped from anatomical acoustic windows (e. g., intercostal and subcostal spaces) to the physical phantom, the corresponding initial joint configurations ($\boldsymbol{q}_{init}$) were specifically searched and predefined. To guarantee statistical reliability, five independent trials were conducted for each of the three control methods at every location. Crucially, all repeated trials were strictly initialized from the exact same $\boldsymbol{q}_{init}$ to eliminate start-state bias, resulting in a total dataset of 90 executions (6 locations × 3 methods × 5 trials).

This deliberate selection of initial joint postures was conducted to establish a unified evaluation standard, ensuring that all comparative control methods are tested under identical kinematic starting conditions. These predefined configurations effectively represent the diverse and often awkward operational postures sonographers must adopt to bypass rib shadowing. From each of these six standardized initial states, the robotic system was tasked with executing the autonomous $\pm 15^{\circ}$ sector sweep defined in Section 2.

3.2. Comparative Methodologies

To benchmark the performance of the proposed methodology, two conventional baseline control strategies—which rely on the manufacturer's standard position-servo interfaces—were implemented for comparison:

Method A: RRT-based Joint Position Servo (RRT-JPS)

This method employs a standard Rapidly exploring Random Tree (RRT) algorithm to plan a collision-free path in the joint space across the discretized scanning waypoints. The resulting trajectory is executed using the robot SDK's joint position servo interface. While globally safe, this sampling-based approach does not analytically enforce the continuous differential constraints of the VPP.

Method B: SDK-based Cartesian Position Servo (SDK-CPS)

This method directly utilizes the robot SDK's Cartesian task-space position servo interface. The $\pm 15^{\circ}$ sector arc is fed directly as a series of 6-DOF pose commands. While this method tracks the Cartesian path, it relies on the manufacturer's "black-box" inverse kinematics, which lacks task-specific null-space optimization (i. e., it does not account for the clinical ergonomics or manipulability defined by our CDSI).

Proposed Method: CDSI-optimized Jacobian Velocity Control (Proposed-JDS)

Our proposed framework, as detailed in Section 2, utilizes offline CDSI optimization to find the optimal arm

angle ψ^*, followed by real-time closed-loop Jacobian redundancy resolution and proportional velocity scaling.

3.3. Evaluation Metrics

To rigorously assess the quality of the robotic sector scan, the performance of each single-motion trajectory was quantified using four time-variant metrics, corresponding to the technical performance profiles illustrated in the results.

- Cartesian Position Tracking Error: Defined as the Euclidean distance between the actual Tool Center Point (TCP) and the desired Virtual Pivot Point (VPP) constraint throughout the sweep. This metric evaluates the system's ability to prevent "tissue slippage", which is critical for maintaining stable acoustic coupling.
- Orientation Tilt Error: Defined as the deviation of the probe's actual scanning plane from the planned reference plane. This error measures the rotational stability (specifically Roll and Yaw deviations) during the sector sweep, ensuring the ultrasound beam captures the intended anatomical cross-section without geometric distortion.
- Task-Specific Directional Manipulability (w_{scan}): A kinematic index measuring the robot's ability to generate velocity specifically along the scanning arc direction. A higher w_{scan} indicates that the robot is operating in a dexterous region far from task-specific singularities, ensuring uniform motion execution without requiring excessive joint velocities.
- Operational Clinical Dexterity & Safety Index (M_{eval}): The performance of the robotic posture during execution is quantified by the Operational CDSI ($\boldsymbol{M_{eval}}$), which integrates clinical ergonomics with a kinematic singularity penalty. Unlike the planning stage, this metric focuses on the instantaneous alignment of the manipulator to maximize clearance from the patient's body.

$$\boldsymbol{M_{eval}(t)} = \sqrt{\boldsymbol{E_{ergo}(t)} + \boldsymbol{P_{sing}(t)}} \tag{28}$$

Clinical Ergonomic Component (E_{ergo}):

To ensure the manipulator maintains a vertical, high-clearance posture (the "elbow-up" configuration), the ergonomic cost penalizes deviations of the pitch joint (q_2) and the subsequent distal joints (q_3,q_4):

$$E_{ergo} = q_2^2 + \cos^2(q_2) \cdot q_3^2 + \sin^2(q_2) \cdot q_4^2 \tag{29}$$

Singularity Penalty Component (P_{sing}):

To prevent the robot from entering configurations where control may be lost or joint velocities may saturate, a penalty function is applied to the joints most susceptible to kinematic singularities (q_2,q_4,q_6):

$$\boldsymbol{P_{sing}} = \boldsymbol{k_{sing}} \sum_{\boldsymbol{i} \in \{2,4,6\}} \frac{1}{\boldsymbol{q_i^2} + \boldsymbol{\epsilon}} \tag{30}$$

q_i: The instantaneous joint angle in degrees (for ergonomics) or radians (for penalty calculation).

k_{sing}: A scaling factor (e.g., 0.005) determining the sensitivity of the singularity avoidance.

ϵ: A small constant (10^{-4}) to prevent numerical division-by-zero errors.

3.4. Results and Discussion

To rigorously evaluate the algorithms, the analysis is divided into two parts: a detailed transient kinematic analysis of a representative posture (Pose 1); an aggregate statistical evaluation demonstrating global robustness across all six clinical poses.

Detailed time-series performance data and joint space trajectories for the remaining five clinical scenarios (Poses 2 through 6) are provided in Appendix A to further substantiate the generalizability of the proposed framework across the entire functional workspace.

3.4.1 Transient Kinematic Analysis (Representative Case: Pose 1)

To understand the dynamic physical behavior and control stability behind the aggregate performance, a detailed time-series analysis was conducted on a single representative trial of Pose 1. Figure 4 illustrates the transient technical performance—comprising Cartesian tracking, orientation stability, manipulability, and operational dexterity—while Figure 5 maps the corresponding joint angle executions.

A. Transient Kinematic Performance (Single-Trial Analysis)

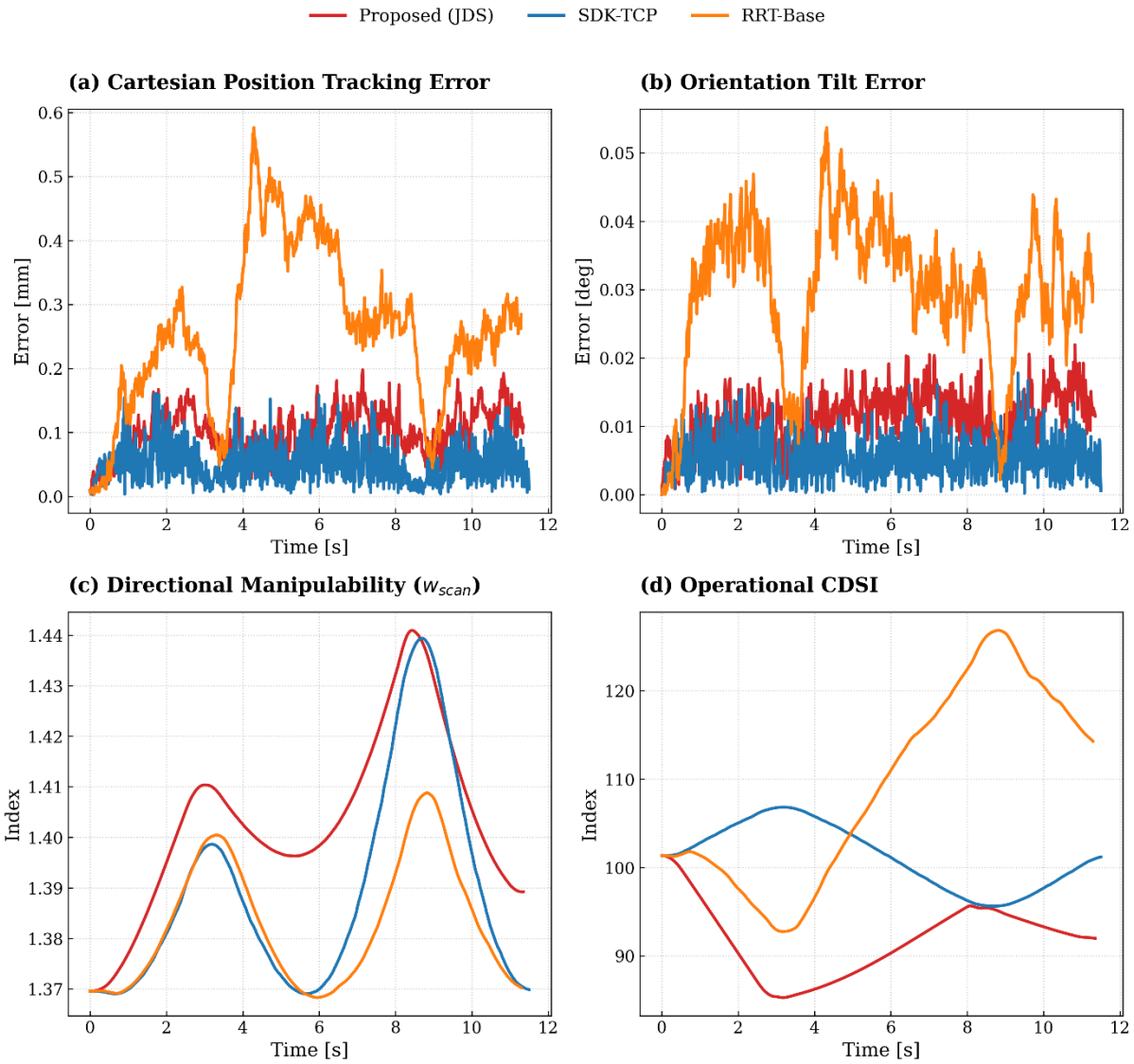

Figure 4. Transient technical performance during the ±15° sector sweep for Pose 1: (**a**) Cartesian position tracking error, (**b**) Orientation tilt error, (**c**) Directional manipulability (ω_{scan}), and (**d**) Operational CDSI evolution.

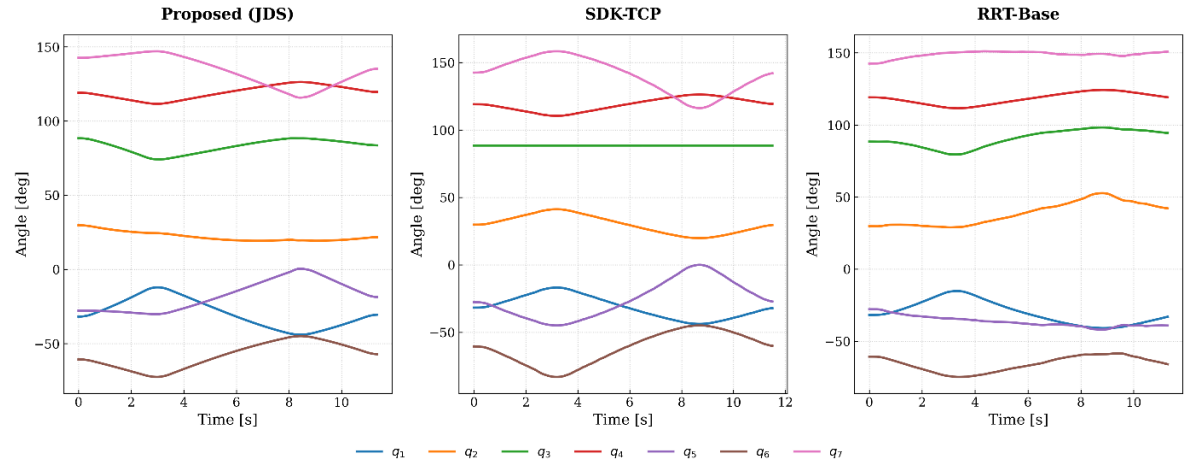

Figure 5. Joint position trajectories over time for Pose 1, comparing (**left**) Proposed JDS, (**center**) SDK-TCP, and (**right**) RRT-Base.

VPP Tracking Accuracy: As shown in Figure 4a, the Proposed JDS method maintains a highly stable

Cartesian tracking profile with a mean error of approximately 0.07 mm. While the SDK-TCP achieves slightly higher "brute-force" precision (0.04 mm), the JDS method stays well within the clinical safety threshold of 0.1 mm. In stark contrast, the RRT-Base method exhibits significant high-frequency chattering, with error spikes frequently exceeding 0.25 mm. This instability in the task space is a direct consequence of the non-smooth, jagged joint trajectories observed in its execution profile (Figure 5, right).

Directional Manipulability (ω_{scan}): In Figure 4c demonstrates that the Proposed JDS ensures superior kinematic conditioning for the scanning task. The JDS method maintains consistently higher ω_{scan} values compared to the baselines. This indicates that the redundant arm is strategically positioned far from singular configurations, providing higher operational margins and smoother execution throughout the scanning arc.

Operational Dexterity: The Operational CDSI (Figure 4d) demonstrates that the JDS controller actively drives the robot toward the most ergonomic "elbow-up" configuration. In contrast, the baseline methods allow the index to fluctuate, indicating a lack of active posture optimization during the sweep.

B. Statistical Stability and Reproducibility (Multi-Trial Summary)

To ensure that the results in Pose 1 are not isolated incidents, five independent trials were conducted under identical initial conditions. The statistical distributions of these trials are visualized in the stability boxplots of Figure 6.

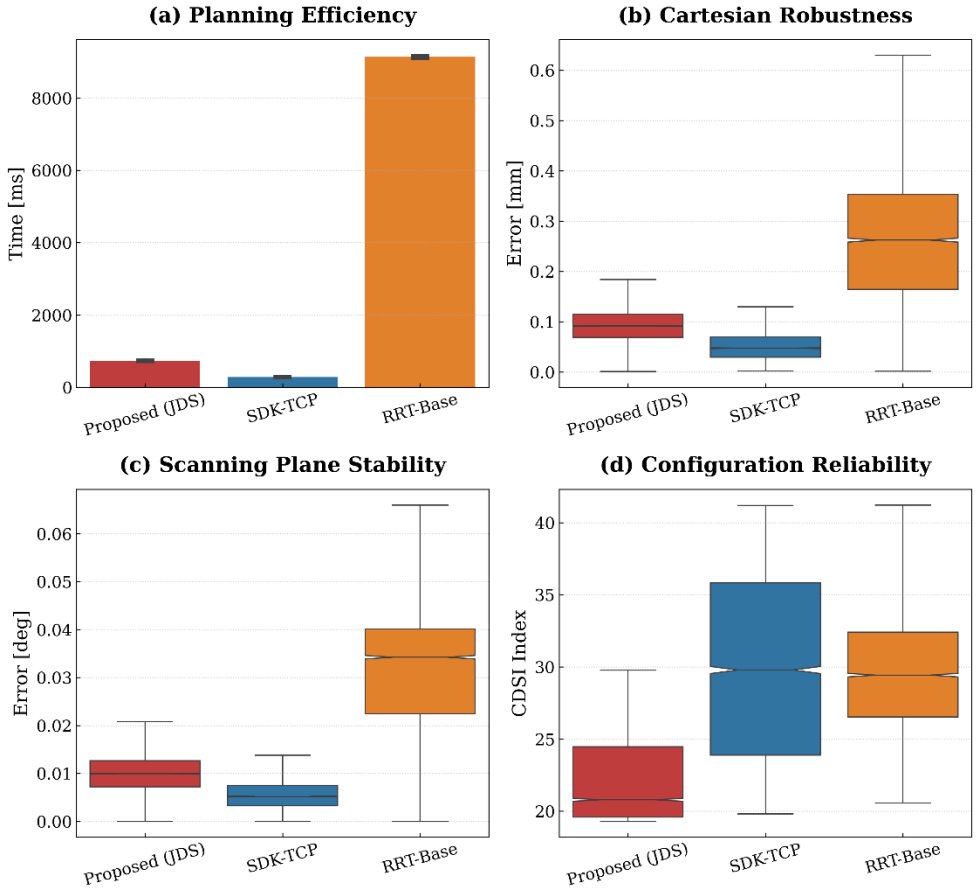

Figure 6. Stability analysis for Pose 1 across 5 repeated trials: (**a**) Planning efficiency, (**b**) Cartesian robustness, (**c**) Tilt error distribution, and (**d**) Clinical Configuration Reliability (CDSI).

Planning Consistency: As shown in Figure 6a, the Proposed JDS exhibits extreme consistency in planning time (722.1 ± 14.2 ms). The negligible variance confirms that the discrete null-space sampling algorithm is numerically stable and provides a predictable sub-second response for clinical workflows.

Tracking Robustness: The Cartesian Tracking Robustness (Figure 6b) and Scanning Plane Stability (Figure 6c) reveal that the Proposed JDS maintains a significantly tighter interquartile range (IQR) for positional error compared to the sampling-based baseline. While SDK-TCP offers higher brute-force precision, the JDS method stays

consistently within the 0.1 mm clinical tolerance. This proves that the velocity-level control law effectively suppresses hardware latency and stochastic noise across multiple runs, ensuring the Virtual Pivot Point (VPP) remains spatially fixed to prevent tissue slippage

Configuration Reliability: The CDSI Index Value distribution (Figure 6d) highlights that our method consistently operates at a lower (more optimal) cost than the RRT-Base. Unlike SDK-TCP, which exhibits a wide spread and higher median cost due to its task-blind redundancy resolution, the Proposed JDS successfully locks the manipulator into the pre-optimized "elbow-up" manifold. This guarantees that the robotic arm repeats the same safe, high-clearance motion profile in every procedure, minimizing the risk of collision with the patient or clinician

3.4.2 Aggregate Performance and Global Robustness Analysis

The aggregate analysis verifies that the advantages observed in the single-trial study are consistently maintained across diverse anatomical challenges. By pooling data from all 90 independent trials (6 poses × 5 trials × 3 methods), we evaluate the system's readiness for varied clinical environments. The quantitative results are summarized in Table 1.

Table 1. Global quantitative comparison of execution metrics across 90 experimental trials.

Method	Plan Time [ms]	Mean Pos Error [mm]	Mean Tilt Error [deg]	Operational Clinical Dexterity (CDSI)	*Motion Smoothness*
Proposed (JDS),	722.1 ± 14.2	0.0730 ± 0.0370	0.0071 ± 0.0036	53.3 ± 25.9	*0.253 ± 0.129*
SDK-TCP	261.4 ± 54.0	0.0390 ± 0.0230	0.0051 ± 0.0029	56.2 ± 28.8	*0.323 ± 0.201*
RRT-Base	7552.7 ± 1598.3	0.141 ± 0.089	0.0199 ± 0.0139	55.5 ± 28.3	*0.262 ± 0.137*

A. Computational Efficiency and Workflow Consistency

Planning efficiency is paramount for intraoperative integration. The RRT-Base method required an average of 7552.7 ms with massive variance (±1598.3 ms), making it unsuitable for high-stakes medical workflows. While SDK-TCP was the fastest (261.4 ms) due to its lack of redundancy optimization, the Proposed JDS achieved a highly efficient planning time of 722.1±14.2 ms. The remarkably low standard deviation confirms that our discrete null-space sampling provides a predictable, sub-second response regardless of the initial probe orientation.

B. Global Tracking Stability and VPP Integrity

Maintaining the Virtual Pivot Point (VPP) without tissue slippage is the primary technical requirement. Table 1 confirms that SDK-TCP achieves the highest Cartesian rigidity (0.0390 mm). The Proposed JDS introduces a marginally higher mean error of 0.0730 mm. the JDS error distribution remains tightly bound and consistently below the 0.1 mm clinical threshold. This microscopic trade-off in absolute rigidity is a deliberate result of the JDS control law, which dynamically prioritizes the secondary task (posture health) within the null-space to actively enforce safety and ergonomics.

C. Clinical Configuration Reliability (CDSI)

The Operational CDSI results differentiate the methods' clinical intelligence. The Proposed JDS achieved the best (lowest) aggregate score of 53.3 ± 25.9, outperforming both the SDK and RRT baselines. By consistently driving the 7-DOF arm toward the "elbow-up" high-clearance manifold, the JDS controller ensures the robot remains in a clinically superior state throughout the sweep. The higher standard deviation across all methods reflects the inherent geometric variety of the six distinct CT-derived poses.

D. Movement Quality and Execution Safety

Safety in medical robotics is intrinsically linked to motion smoothness. The Proposed JDS demonstrated the highest execution quality with an aggregate Jerk value of 0.253 ± 0.129, significantly lower than SDK-TCP

(0.323 ± 0.201). Although SDK-TCP is locally precise, its lack of global redundancy foresight leads to transient accelerations (internal "self-motions") when maintaining poses near singular regions. In contrast, the JDS method utilizes the globally optimized ψ^* as a continuous attractive manifold, resulting in fluid joint transitions and reduced vibration, which is critical for preserving ultrasound image quality.

4. Conclusions and Future Work

4.1. Conclusions

This study presented a hierarchical motion control framework for automating ultrasound sector scanning using a redundant 7-DOF robotic manipulator. The primary objective was to resolve the complex kinematic redundancy in a way that guarantees clinical safety and dexterity while executing precise sector sweeps within constrained anatomical windows (e.g., intercostal spaces).

The proposed methodology integrates a global offline planning stage with a real-time execution stage. In Stage 1, a novel Clinical Dexterity & Safety Index (CDSI) was developed to globally optimize the redundant arm angle (ψ^*), ensuring the robot operates far from kinematic singularities and joint limits. In Stage 2, a Jacobian-based Redundancy Resolution (JDS) controller with proportional velocity scaling was implemented to execute the planned motion. This controller dynamically projects the optimized posture into the null space of the primary scanning task, ensuring real-time compliance with the Virtual Pivot Point (VPP) constraint.

Comprehensive experiments based on six pre-operative CT-derived clinical poses were conducted on a tissue-mimicking phantom. The proposed framework was benchmarked against two standard baselines: an RRT-based joint position servo (RRT-JPS) and a manufacturer-provided Cartesian servo (SDK-CPS). The quantitative results demonstrate that:

Superior Smoothness and Safety: The proposed JDS method achieved the smoothest joint velocity profiles (lowest jerk), effectively eliminating the hazardous high-frequency vibrations observed in sampling-based methods and the unpredictable self-motions seen in unconstrained solvers.

Clinical Ergonomics: By actively enforcing the CDSI-optimized posture via null-space projection, the system consistently maintained an "elbow-up" configuration with high manipulability, whereas baseline methods frequently allowed the manipulator to drift into sub-optimal or near-singular states.

Sub-millimeter Precision: Although the SDK-CPS method achieved marginally lower Cartesian positioning error (0.039 mm vs. 0.073 mm), the proposed method maintained VPP tracking error well within the clinical tolerance (<0.1 mm). This slight trade-off in absolute rigidity yielded a significant gain in overall system safety and predictability.

Operational Efficiency: The algorithm achieved a sub-second planning time (<800 ms), making it highly suitable for integration into real-time intraoperative workflows.

In conclusion, the proposed framework successfully bridges the gap between geometric path planning and compliant dynamic control, offering a robust solution for standardizing robotic ultrasound interventions in complex anatomical environments.

4.2. Future Work

While the current results are promising, several avenues for future research are identified to further enhance the clinical applicability of the system:

Force-Admittance Control for Soft Tissue Interaction:

The current validation was performed on a rigid phantom setup. In real clinical scenarios, the interaction forces between the ultrasound probe and the patient's soft tissue are critical for image quality. Future work will integrate a force/torque sensor at the end-effector. An admittance control loop will be superimposed on the current JDS framework to regulate the contact force (z-axis) dynamically, compensating for tissue deformation while maintaining the VPP constraint.

Respiratory Motion Compensation:

The liver is subject to significant displacement due to respiration. To address this, we plan to implement a

visual serving mechanism or an external optical tracking system to monitor the patient's respiratory cycle in real-time. The target VPP position $\boldsymbol{p}_{vpp}$ will be dynamically updated in the control loop, allowing the robot to actively compensate for physiological motion and maintain the target acoustic window.

Dynamic Obstacle Avoidance:

The current offline planning assumes a static environment. Future iterations will incorporate depth cameras (RGB-D) to detect dynamic obstacles (e.g., surgical staff or other equipment) in the operating room. The null-space projection term in the JDS controller will be expanded to include a collision repulsion vector, enabling the robot to autonomously reconfigure its elbow to avoid collisions without interrupting the scanning task.

Funding

This research received no external funding.

Author Contributions

Writing—original draft, P.C., H.Y. and B.Z.; writing—review and editing, P.C., H.Y. and B.Z. All authors have read and agreed to the published version of the manuscript.

Institutional Review Board Statement

Not applicable. This study did not involve humans or animals. All experimental validations and performance evaluations were conducted using a synthetic tissue-mimicking phantom and de-identified pre-operative medical imaging data.

Informed Consent Statement

Not applicable. This study did not involve human subjects. All experimental validations were performed using a synthetic tissue-mimicking phantom.

Data Availability Statement

Not applicable. This study does not report any data involving identifiable human participants.

Conflicts of Interest

The authors declare no conflict of interest.

Abbreviations

The following abbreviations are used in this manuscript:

JDS	Jacobian-based Redundancy Resolution
VPP	Virtual Pivot Point
CDSI	Clinical Dexterity & Safety Index
DOF	Degrees of Freedom
RUSS	Robotic Ultrasound Scanning Systems
US	Ultrasound

Appendix A

Appendix A.1

As discussed in Section 3.4, to preserve the narrative flow of the main text, the detailed transient kinematic

analysis and joint trajectory profiles were presented for a single representative clinical posture (Pose 1). This appendix provides the comprehensive supplementary data for the remaining five pre-operatively planned initial scanning poses (Poses 2 through 6). These supplementary figures validate the reproducibility, robustness, and clinical reliability of the proposed CDSI-optimized JDS control framework across the diverse spectrum of spatial orientations required to navigate narrow intercostal acoustic windows during ultrasound-guided liver interventions.

Appendix A.2. Transient Technical Performance (Poses 2–6)

The transient performance metrics during the continuous ±15° sector sweep for Poses 2 through 6 are illustrated in Figures A1 to A5. Each figure comprises four subplots detailing: (a) the Cartesian Virtual Pivot Point (VPP) tracking error, demonstrating the spatial rigidity of the proposed method; (b) the orientation tilt error; (c) the task-specific manipulability, highlighting the avoidance of kinematic singularities; and (d) the real-time evolution of the Clinical Dexterity & Safety Index (CDSI) score. Consistent with the findings in the main text, the Proposed JDS method maintains a bounded Cartesian error while continuously driving the manipulator toward the optimal ergonomic state.

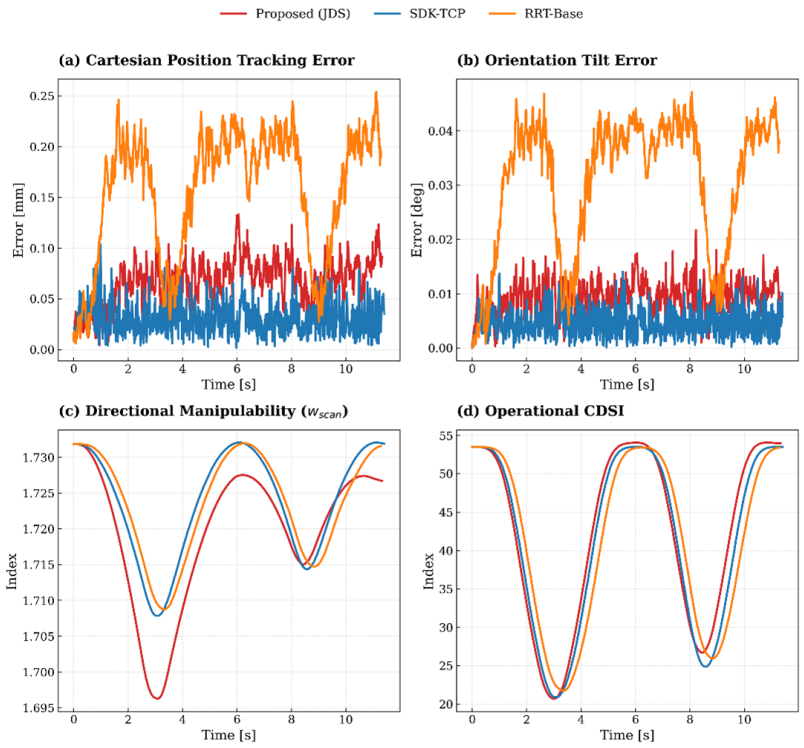

Figure A1. Transient technical performance during the sector sweep for Pose 2, comparing the Proposed JDS, SDK-TCP, and RRT-Base methods.

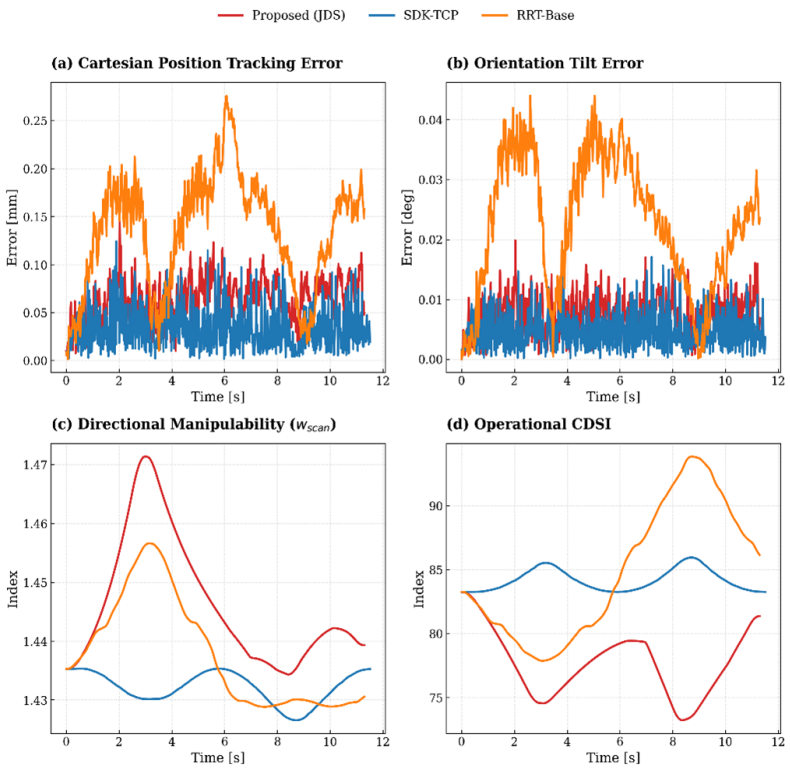

Figure A2. Transient technical performance during the sector sweep for Pose 3, comparing the Proposed JDS, SDK-TCP, and RRT-Base methods.

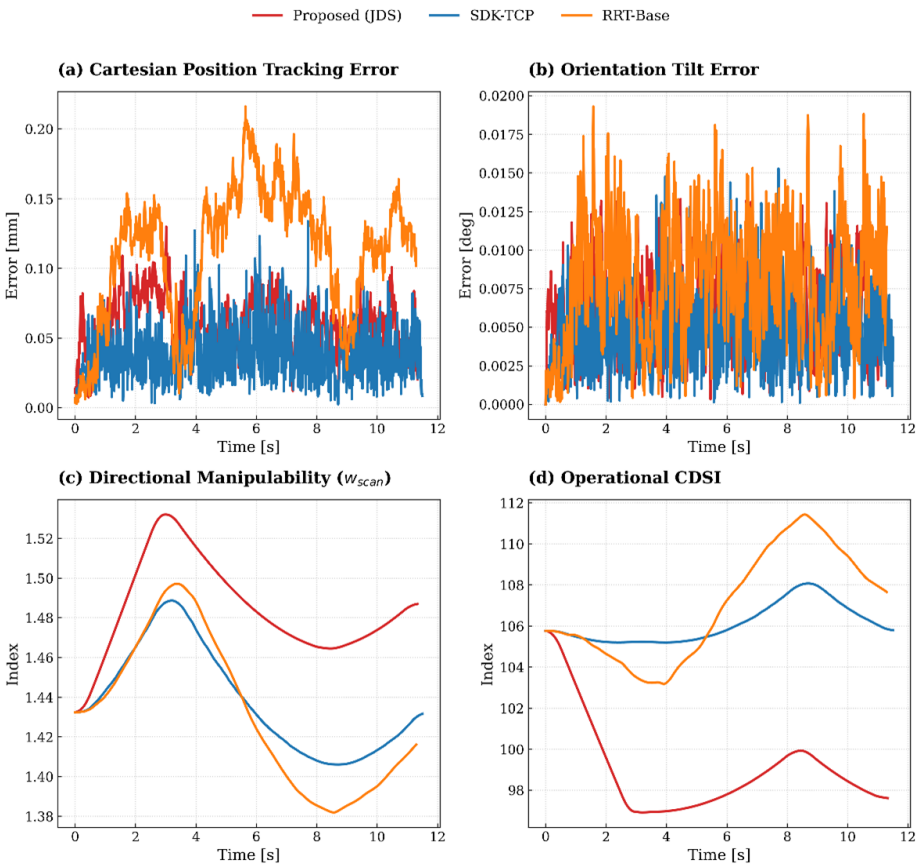

Figure A3. Transient technical performance during the sector sweep for Pose 4, comparing the Proposed JDS, SDK-TCP, and RRT-Base methods.

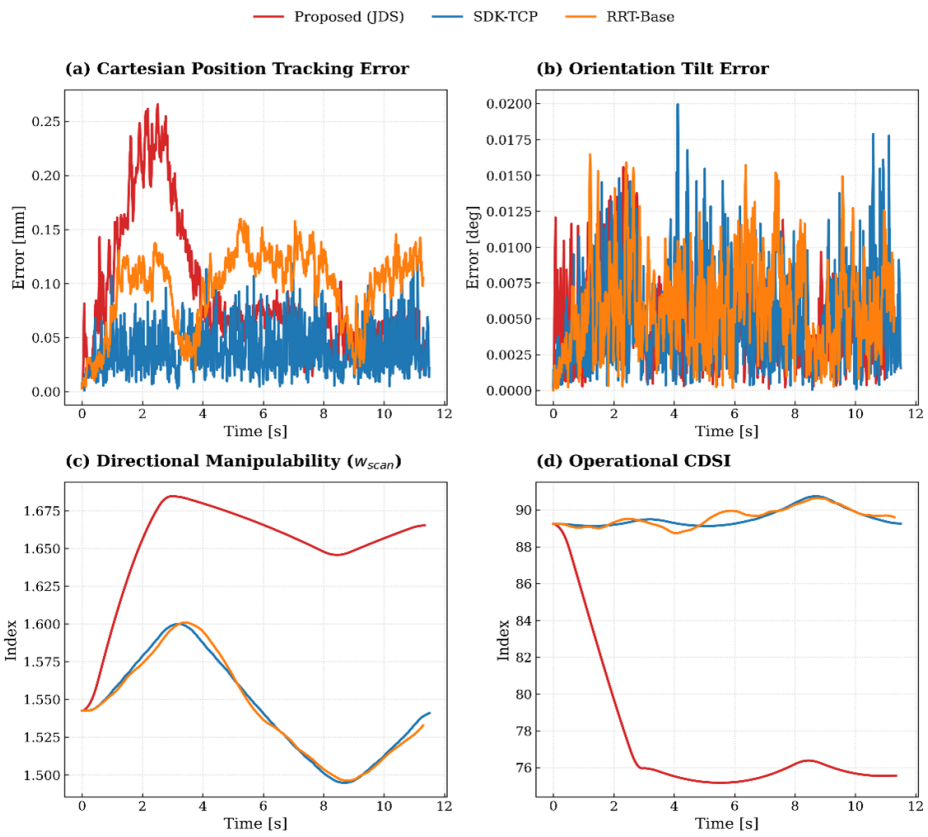

Figure A4. Transient technical performance during the sector sweep for Pose 5, comparing the Proposed JDS, SDK-TCP, and RRT-Base methods.

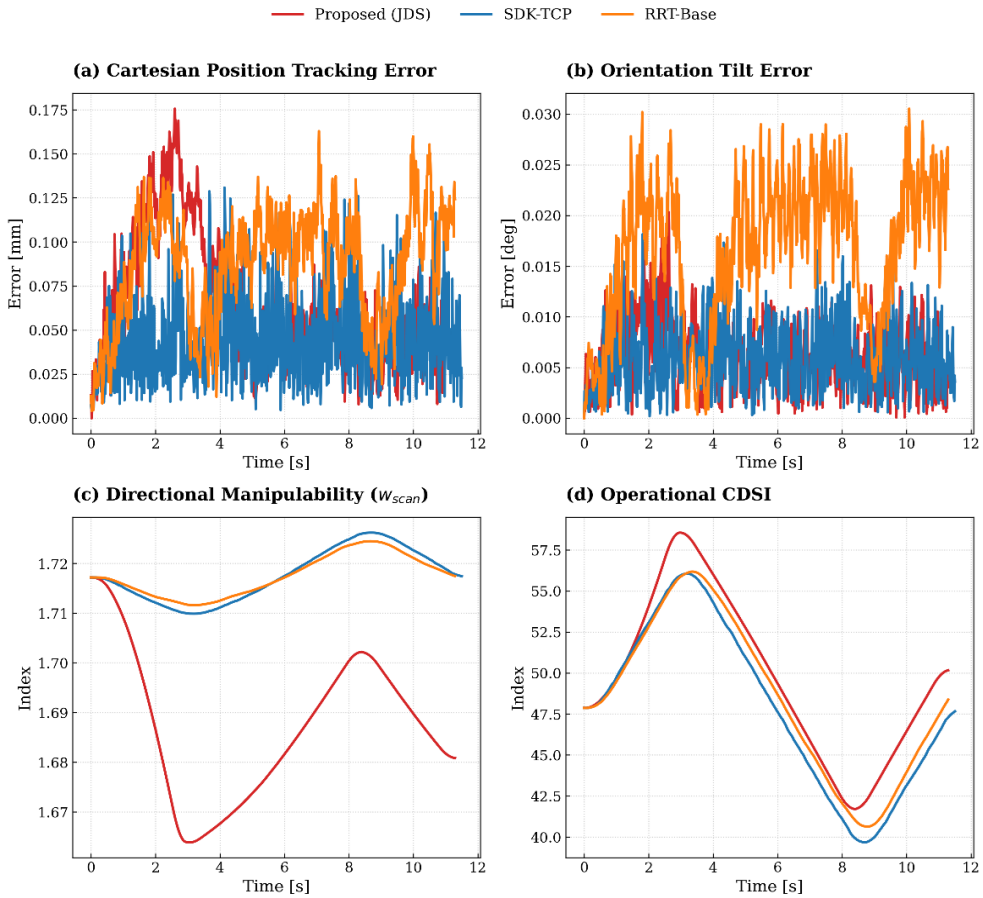

Figure A5. Transient technical performance during the sector sweep for Pose 6, comparing the Proposed JDS, SDK-TCP, and RRT-Base methods.

Appendix A.3. Joint Space Execution and Smoothness (Poses 2–6)

The safety of physical human-robot interaction in surgical environments relies heavily on the continuity of joint velocities. Figures A6 to A10 present the time-series joint position trajectories (q^1 through q^7) for the baseline and proposed methods across the remaining clinical poses. The data demonstrates that the Proposed JDS framework effectively eliminates the high-frequency chattering observed in sampling-based approaches (RRT-Base) and the sudden internal self-motions characteristic of unconstrained inverse kinematics solvers (SDK-TCP).

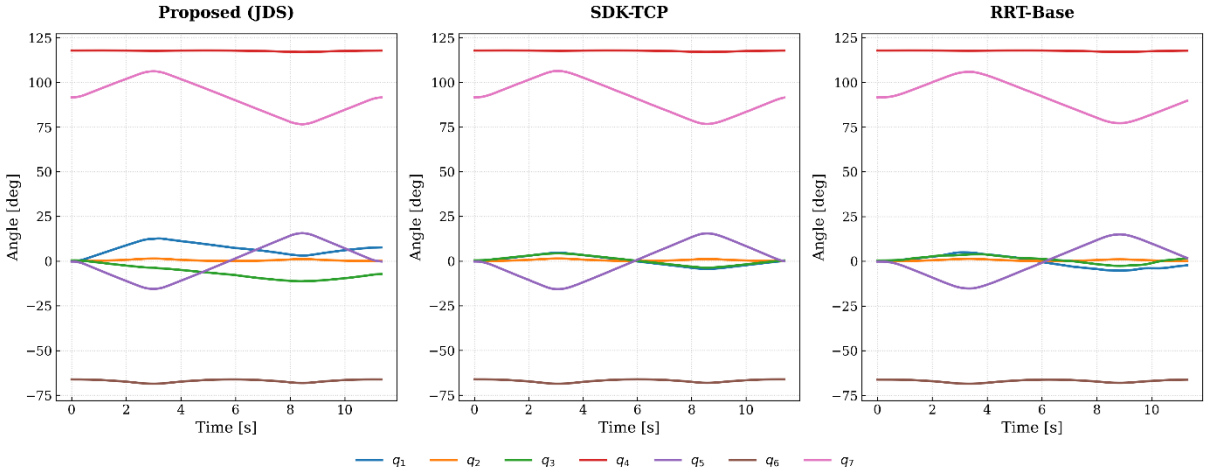

Figure A6. Joint position trajectories over time for Pose 2.

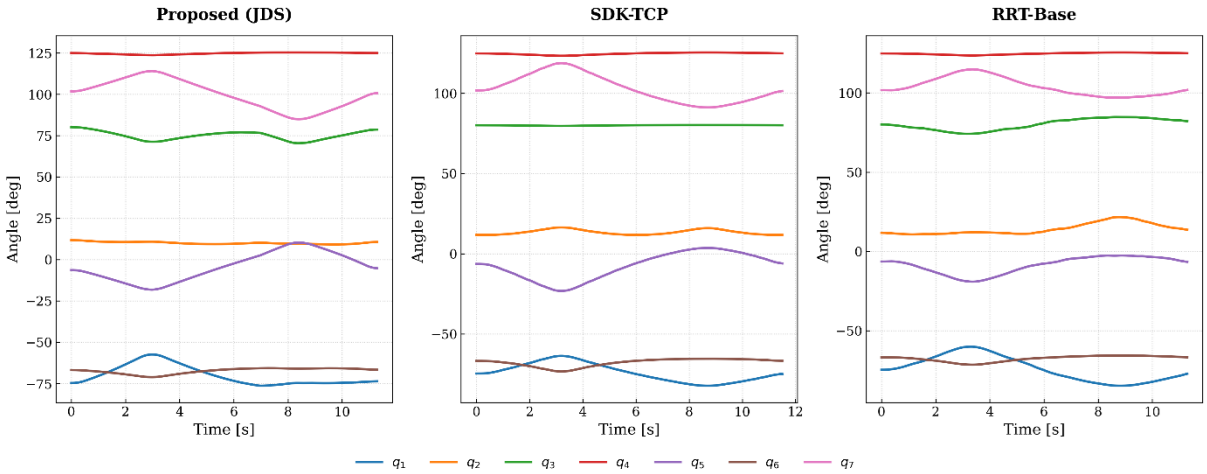

Figure A7. Joint position trajectories over time for Pose 3.

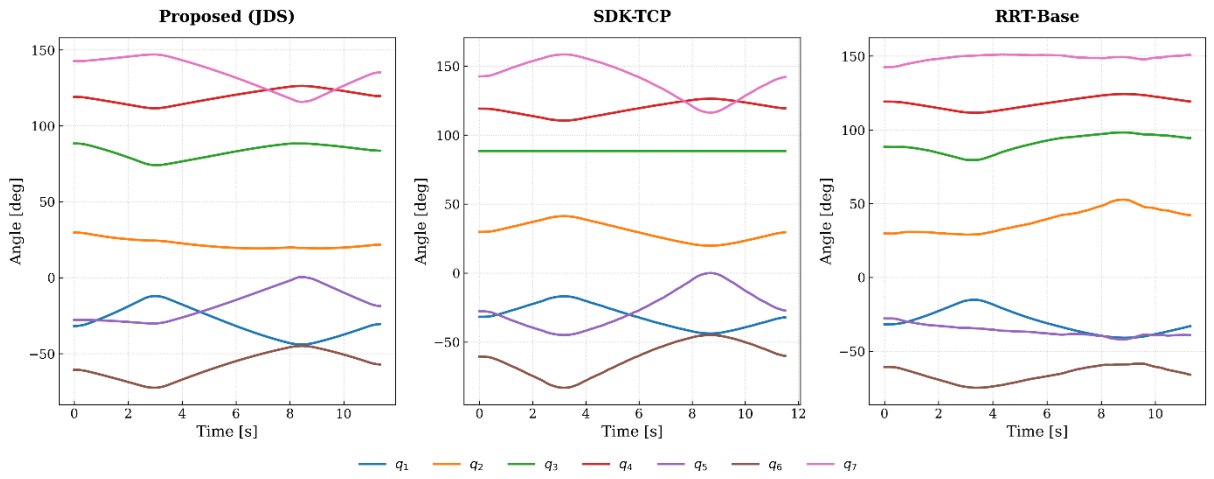

Figure A8. Joint position trajectories over time for Pose 4.

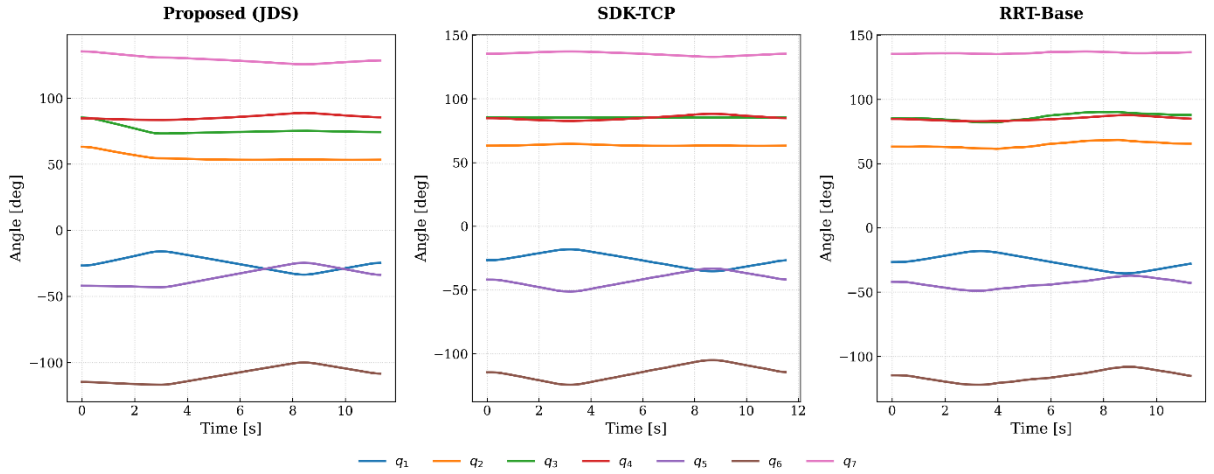

Figure A9. Joint position trajectories over time for Pose 5.

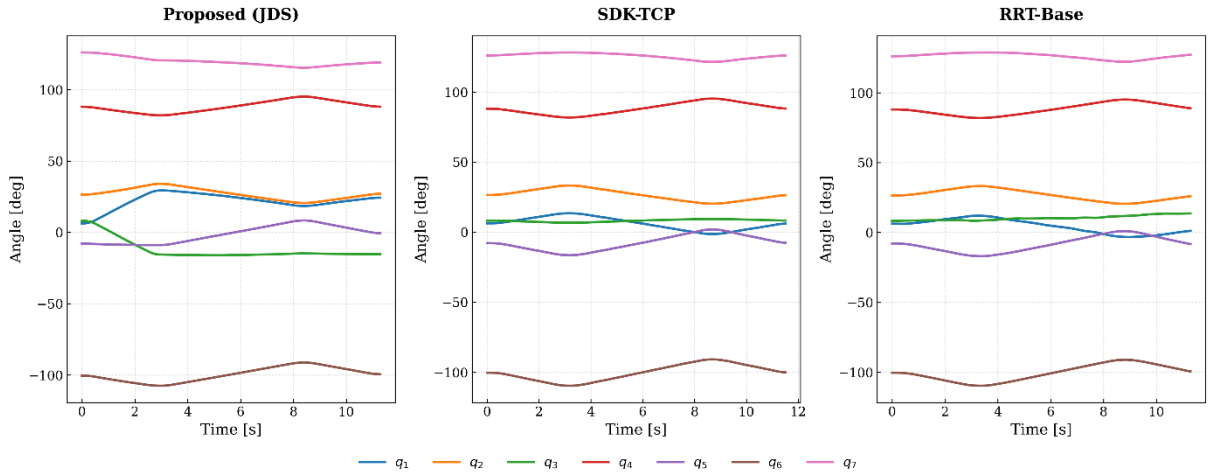

Figure A10. Joint position trajectories over time for Pose 6.

Appendix A.4. Stability and Distribution Analysis

To further substantiate the statistical findings summarized in Table 1 of the main text, Figures A11 to A15 provide the boxplot distributions of the execution metrics for Poses 2 through 6. These distributions confirm that the sub-second planning efficiency, sub-millimeter tracking accuracy, and superior clinical dexterity of the Proposed JDS framework are not isolated to a specific favorable initial posture but are mathematically

guaranteed across the operational workspace.

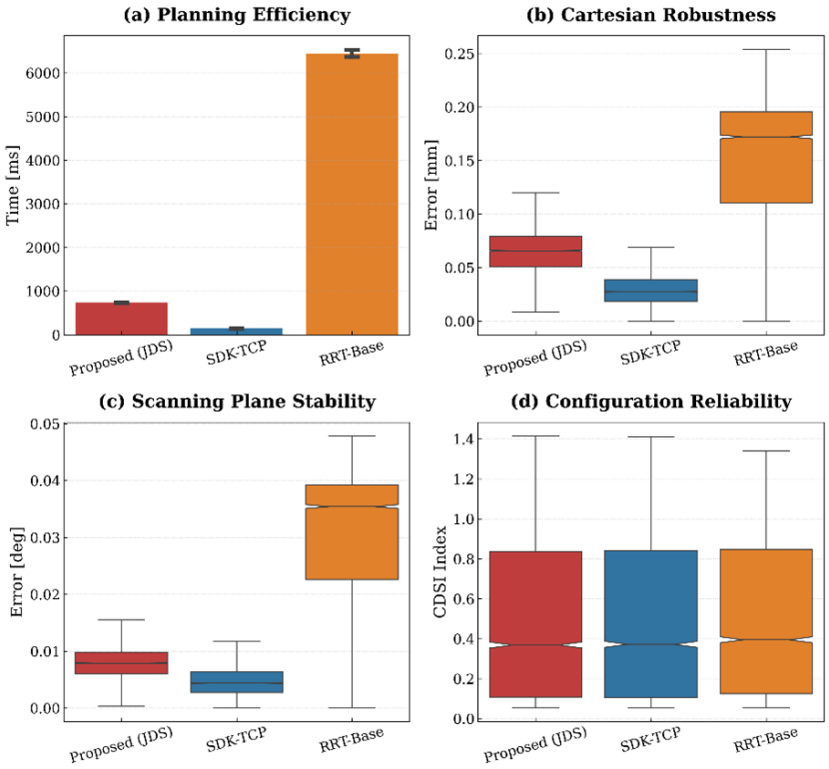

Figure A11. Aggregate stability analysis boxplots for Pose 2, detailing the distribution of tracking errors, CDSI scores.

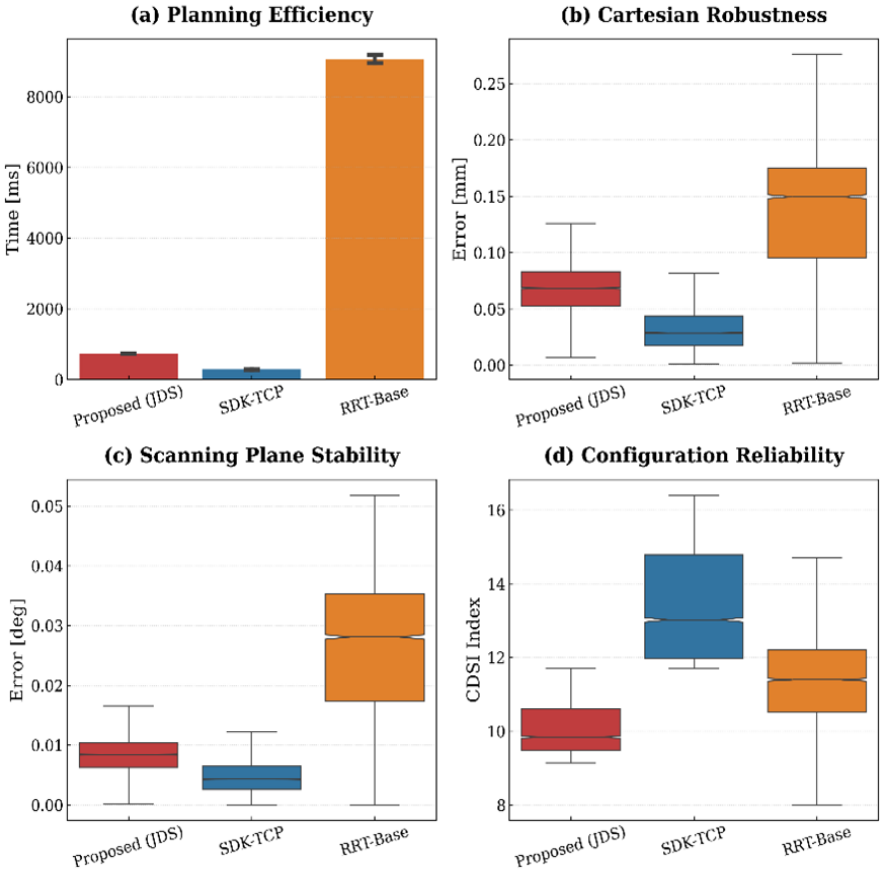

Figure A12. Aggregate stability analysis boxplots for Pose 3, detailing the distribution of tracking errors, CDSI scores.

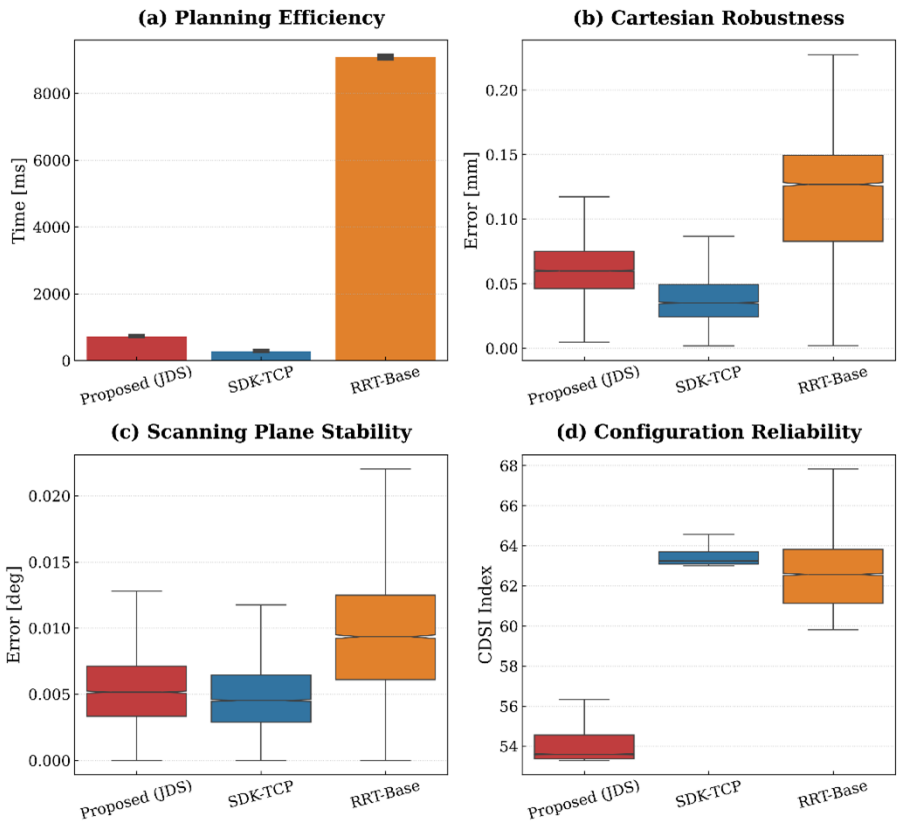

Figure A13. Aggregate stability analysis boxplots for Pose 4, detailing the distribution of tracking errors, CDSI scores.

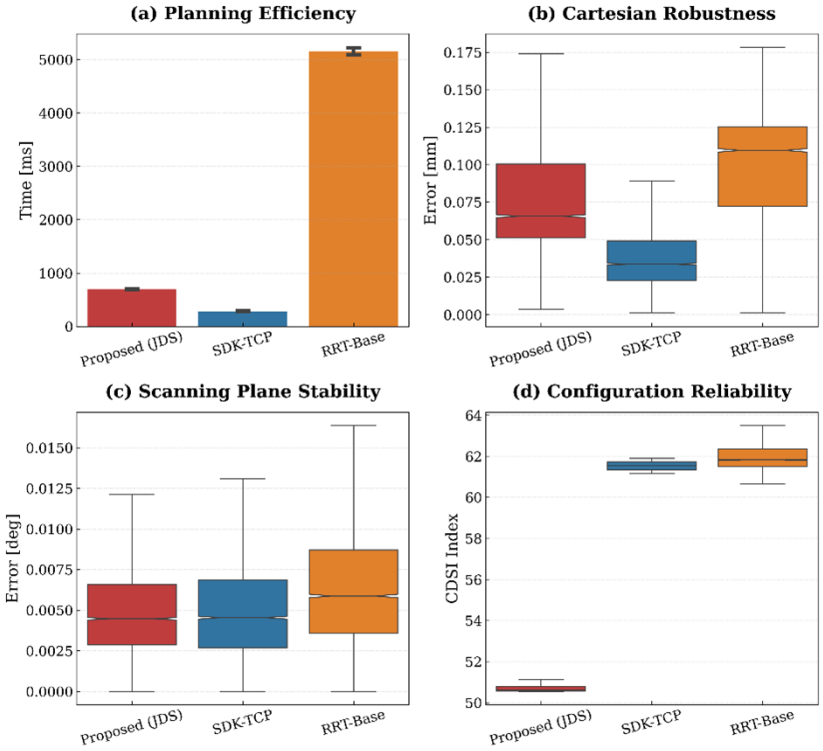

Figure A14. Aggregate stability analysis boxplots for Pose 5, detailing the distribution of tracking errors, CDSI scores.

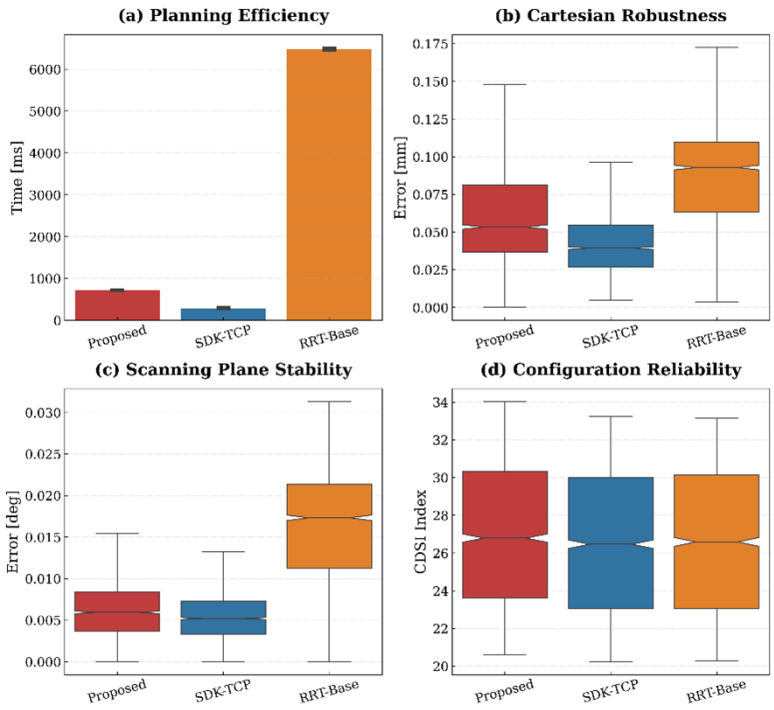

Figure A15. Aggregate stability analysis boxplots for Pose 6, detailing the distribution of tracking errors, CDSI scores.

References

1 Yang T, Chen Q, Kuang L, *et al.* Effectiveness and Safety of Ultrasound-Guided High-Intensity Focused Ultrasound Ablation for the Treatment of Colorectal Cancer Liver Metastases. *International Journal of Hyperthermia* 2022; **39**: 829–834. https://doi.org/10.1080/02656736.2022.2086712.

2 Li N, Dong Y, Ding Y, *et al.* Comparison of the Efficacy and Safety of Ultrasound-Guided Radiofrequency Ablation and Microwave Ablation for the Treatment of Unifocal Papillary Thyroid Microcarcinoma: A Retrospective Study. *International Journal of Hyperthermia* 2024; **41**: 2287964. https://doi. org/10.1080/02656736.2023.2287964.

3 Cheng Z, Koskinopoulou M, Bano S, *et al.* Sensing Technologies for Guidance During Needle-Based Interventions. *IEEE Transactions on Instrumentation and Measurement* 2024; **73**: 4009615. https://doi.org/10.1109/TIM.2024.3441017.

4 Long Y, Xu E, Zeng Q, *et al.* Intra-Procedural Real-Time Ultrasound Fusion Imaging Improves the Therapeutic Effect and Safety of Liver Tumor Ablation in Difficult Cases. *American Journal of Cancer Research* 2020; **10**: 2174–2184.

5 Lin XX, Li MD, Ruan SM, *et al.* Autonomous Robotic Ultrasound Scanning System: A Key to Enhancing Image Analysis Reproducibility and Observer Consistency in Ultrasound Imaging. *Frontiers in Robotics and AI* 2025; **12**: 1527686. https://doi.org/10.3389/frobt.2025.1527686.

6 Kennedy VL, Flavell CA, Doma K. Intra-Rater Reliability of Transversus Abdominis Measurement by a Novice Examiner: Comparison of “Freehand” to “Probe Force Device” Method of Real-Time Ultrasound Imaging. *Ultrasound* 2019; **27**: 156–166. https://doi.org/10.1177/1742271X19831720.

7 Penzkofer T, Bruners P, Isfort P, *et al.* Free-Hand CT-Based Electromagnetically Guided Interventions: Accuracy, Efficiency and Dose Usage. *Minimally Invasive Therapy & Allied Technologies* 2011; **20**: 226–233. https://doi.org/10.3109/13645706.2011.553256.

8 Jung EM, Friedrich C, Hoffstetter P, *et al.* Volume Navigation with Contrast Enhanced Ultrasound and Image Fusion for Percutaneous Interventions: First Results. *PLoS ONE* 2012; **7**: e33956. https://doi.org/10.1371/journal.pone.0033956.

9 Munir K, Al-Battal AF, Alsheghri A, *et al.* A Survey of Autonomous Robotic Ultrasound Scanning Systems. *IEEE Access* 2025; **13**: 103178–103197. https://doi.org/10.1109/ACCESS.2025.3574464.

10 Suligoj F, Heunis CM, Sikorski J, *et al.* RobUSt–An Autonomous Robotic Ultrasound System for Medical Imaging. *IEEE Access* 2021; **9**: 67456–67465. https://doi.org/10.1109/ACCESS.2021.3077037.

11 Ginhoux R, Gangloff J, de Mathelin M, *et al.* Active Filtering of Physiological Motion in Robotized Surgery Using Predictive Control. *IEEE Transactions on Robotics* 2005; **21**: 67–79. https://doi.org/10.1109/TRO.2004.833812.

12 Jiang Z, Grimm M, Zhou M, *et al.* Automatic Force-Based Probe Positioning for Precise Robotic Ultrasound Acquisition. *IEEE Transactions on Industrial Electronics* 2021; **68**: 11200–11211. https://doi.org/10.1109/TIE.2020.3036215.

13 Xie Z, Jin L, Luo X. Kinematics-Based Motion-Force Control for Redundant Manipulators with Quaternion Control. *IEEE Transactions on Automation Science and Engineering* 2023; **20**: 1815–1828. https://doi.org/10.1109/TASE.2022.3186668.

14 Chatelain P, Krupa A, Navab N. Confidence-Driven Control of an Ultrasound Probe. *IEEE Transactions on Robotics* 2017; **33**: 1410–1424. https://doi.org/10.1109/TRO.2017.2723618.

15 Wang Z, Zhao B, Zhang P, *et al.* Full-Coverage Path Planning and Stable Interaction Control for Automated Robotic Breast Ultrasound Scanning. *IEEE Transactions on Industrial Electronics* 2023; **70**: 7051–7061. https://doi.org/10.1109/TIE.2022.3204967.

16 Duan B, Xiong L, Guan X, *et al.* Tele-Operated Robotic Ultrasound System for Medical Diagnosis. *Biomedical Signal Processing and Control* 2021; **70**: 102900. https://doi.org/10.1016/j.bspc.2021.102900.

17 Torres LG, Baykal C, Alterovitz R. Interactive-Rate Motion Planning for Concentric Tube Robots. In Proceedings of the 2014 IEEE International Conference on Robotics and Automation (ICRA), Hong Kong, China, 31 May–7 June 2014; pp. 1915–1921.

18 Fiore MD, Meli G, Ziese A, *et al.* A General Framework for Hierarchical Redundancy Resolution Under Arbitrary Constraints. *IEEE Transactions on Robotics* 2023; **39**: 2468–2487. https://doi.org/10.1109/TRO.2022.3232266.

19 Pagnotta DP, Monteriù A, Freddi A, *et al.* Redundancy Resolution Scheme for Manipulators Subject to Inequality Constraints. *International Journal of Control, Automation and Systems* 2023; **21**: 575–590. https://doi.org/10.1007/s12555-021-0641-8.

20 Zhang B, Chen K, Yao Y, *et al.* Semi-Automatic Puncture Robotic System Based on Real-Time Multi-Modal Image Fusion: Preclinical Evaluation. *International Journal of Computer Assisted Radiology and Surgery* 2025; **20**: 2479–2489. https://doi.org/10.1007/s11548-025-03471-5.

21 Albu-Schäffer A, Haddadin S, Ott C, *et al.* The DLR Lightweight Robot: Design and Control Concepts for Robots in Human Environments. *Industrial Robot* 2007; **34**: 376–385. https://doi.org/10.1108/01439910710774386.

22 Li K, Xu Y, Meng MQH. An Overview of Systems and Techniques for Autonomous Robotic Ultrasound Acquisitions. *IEEE Transactions on Medical Robotics and Bionics* 2021; **3**: 510–524. https://doi.org/10.1109/TMRB.2021.3072190.

23 Su K, Liu J, Ren X, *et al.* A Fully Autonomous Robotic Ultrasound System for Thyroid Scanning. *Nature Communications* 2024; **15**: 4004. https://doi.org/10.1038/s41467-024-48421-y.

24 Wein W, Brunke S, Khamene A, *et al.* Automatic CT-Ultrasound Registration for Diagnostic Imaging and Image-Guided Intervention. *Medical Image Analysis* 2008; **12**: 577–585. https://doi.org/10.1016/j.media.2008.06.006.

25 Shimizu M, Kakuya H, Yoon WK, *et al.* Analytical Inverse Kinematic Computation for 7-DOF Redundant Manipulators with Joint Limits and Its Application to Redundancy Resolution. *IEEE Transactions on Robotics* 2008; **24**: 1131–1142. https://doi.org/10.1109/TRO.2008.2003266.

26 Wiedmeyer W, Altoé P, Auberle J, *et al.* A Real-Time-Capable Closed-Form Multi-Objective Redundancy Resolution Scheme for Seven-DoF Serial Manipulators. *IEEE Robotics and Automation Letters* 2021; **6**: 431–438. https://doi.org/10.1109/LRA.2020.3045646.

27 Tsai CC, Hung CC, Chang CF. Trajectory Planning and Control of a 7-DOF Robotic Manipulator. In Proceedings of the 2014 International Conference on Advanced Robotics and Intelligent Systems (ARIS),

Taipei, Taiwan, 6–8 June 2014; pp. 78–84.